# UV Observations of Prominence Activation and Cool Loop Dynamics

T.A. Kucera

*NASA's Goddard Space Flight Center, Code 612.1, Greenbelt, MD 20771*

`Therese.A.Kucera@nasa.gov`

and

E. Landi

*Artep, Inc., Ellicott City, MD 21402 and*
*Naval Research Laboratory, Washington, DC 20375-5320*

## Abstract

In this paper we investigate the thermal and dynamic properties of dynamic structures in and around a prominence channel observed on the limb on 17 April 2003. Observations were taken with the *Solar and Heliospheric Observatory's* Solar Ultraviolet Measurements of Emitted Radiation (*SOHO*/SUMER) in lines formed at temperatures from 80,000 to 1.6 MK. The instrument was pointed to a single location and took a series of 90 s exposures. Two-dimensional context was provided by the *Transition Region and Coronal Explorer* (*TRACE*) in the UV and EUV and the Kanzelhöhe Solar Observatory in Hα. Two dynamic features were studied in depth: an activated prominence and repeated motions in a loop near the prominence. We calculated three-dimensional geometries and trajectories, differential emission measure, and limits on the mass, pressure, average density, and kinetic and thermal energies. These observations provide important tests for models of dynamics in prominences and cool ($\sim 10^5$ K) loops, which will ultimately lead to a better understanding the mechanism(s) leading to energy and mass flow in these solar features.

## 1. Introduction

Observations of plasmas in the solar atmosphere at $\log T(\mathrm{K}) \lesssim 5$ show a highly dynamic environment, with features flickering in and out of view in tens of minutes and material moving at tens or even hundreds of km s$^{-1}$. In this paper we analyze two examples of dynamic motion commonly seen at these "transition region" temperatures: a motion in a activated prominence and an inhomogeneous flow in a cool loop associated with the prominence. Both were located in a plage region on the solar limb. We analyzed high cadence data ($\gtrsim 1$ image/90 s) from both an imager and a spectrograph observing in the UV and EUV along with ground-based Hα imagery, allowing

us to measure physical parameters with which to test models of solar atmospheric dynamics. Such tests are needed if we are to obtain a better understanding of what causes the dynamics observed at these temperatures.

Studies of even the stable, large-scale prominences in quiet areas of the Sun show that the $\log T(\mathrm{K}) \approx 4$ plasmas of which they are chiefly comprised are flowing in complex counter-streaming patterns with velocities up to about 15 km s$^{-1}$ (Zirker et al. 1998; Lin, Engvold, & Wiik 2003). In addition to these chromospheric temperature plasmas, prominences regularly produce emission at temperatures up to about $\log T(\mathrm{K}) \approx 5.5$. A number of observations of prominences at such temperatures show motions of up to 70 km s$^{-1}$ (Wang 1999; Pojoga & Molowny-Horas 1999; Kucera et al. 2003). Such higher velocities seen in H$\alpha$ are thought to be evidence that extra energy is being inserted into the prominence, an event referred to as an "activation." It has been suggested that activation events in the form of upward moving jets of plasma may be the mechanism for insertion of mass into prominences (Chae et al. 2000a; Chae 2003).

Observations of transition-region temperature loops have also shown them to be highly dynamic structures, far more variable and active than the usually larger, more stable coronal ($\log T(\mathrm{K}) \gtrsim 6$) loops. Doppler measurements made with the *Solar and Heliospheric Observatory* (*SOHO*)'s Coronal Diagnostic Spectrometer (CDS) and Solar Ultraviolet Measurements of Emitted Radiation (SUMER) spectrographs show Doppler velocities of over 300 km s$^{-1}$ (Brekke et al. 1997; Kjeldseth-Moe & Brekke 1998), although they are typically below 200 km s$^{-1}$. The flows can be downwards from the loop apex, but often flow from loop footpoint to footpoint (e.g., Spadaro et al. 2000). Chae et al. (2000b) report rotational motion around loop axes. Loops in this temperature regime change and even appear and disappear on time scales of a few tens of minutes or less. (Fredvik et al. 2002; Di Giorgio, Reale, & Peres 2003). Using the *Transition Region and Coronal Explorer* (*TRACE*) imager, Schrijver (2001) found loops exhibiting cool downflows which were apparently due to cooling and condensing of material seen at coronal temperatures.

Various theories have been put forth to explain the dynamic motions in prominences and transition-region temperature loops, and in some cases the same or similar theories have been applied to both kinds of feature. The purpose of this work is to provide quantitative measurements of physical parameters on time scales necessary to study features moving at a few tens of km s$^{-1}$ or faster. To do this we must combine the capabilities of both spectroscopic and imaging instruments.

Currently available solar spectrometers are relatively slow to produce two dimensional images. In the spectroscopic studies mentioned above, 2D rasters were constructed over at least 10 minutes and sometimes as long as an hour, making it difficult to truly study dynamic features on the necessary time scales. However, spectrographs, with their excellent spectral and thus temperature resolution and ability to measure line diagnostics, offer unique capabilities necessary for measuring the physical properties of plasmas. In order to use spectrographs to study dynamic behavior at short time scales we are combining high-cadence spectroscopic observations from SUMER (taken with the slit in a single location off disk) with high-cadence 2D imagery from *TRACE* and, when

available, ground-based Hα data from Kanzelhöhe Solar Observatory (KSO).

This combination of data allows us to analyze quickly moving features and determine their trajectories, velocities, rate of recurrence, and differential emission measures, as well as limits on their densities, mass, pressure, kinetic and thermal energies, and filling factors. These are important quantities for testing well-developed models for dynamic behavior in this temperature regime.

In the following section we describe the observations and basic data reduction. Section 3 describes the data analysis, with the results presented in §4. In §5 we discuss these results and their bearing on some of the current models of dynamics in the solar atmosphere.

## 2. Observations and Data Reduction

The prominence analyzed in this study was located in an area of plage about 11° south of the heliospheric equator. As it crossed the meridian on 2003 April 10 it displayed an "S" shape with top and bottom segments running roughly east-west and a more north-south oriented central portion. Another filament was positioned about 12° further south and was roughly parallel with the other filament, running from south-east to north-west. On April 17 this second filament was also in the *TRACE* field of view, but was not covered by the SUMER slit.

Paris-Meudon Observatory reports a sudden disappearance of a portion of the northern filament on April 8 and of a part of the southern filament on April 10, but no notable activity between those dates and April 17. On April 18 the area produced a prominence eruption associated with a CME. Meudon Spectroheliograph and *SOHO*/Extreme ultraviolet Imaging Telescope (EIT) data show activity from the region during the event, but it is difficult to tell which of the filaments was involved because they had rotated over the limb.

The transition-region temperature loop discussed in this paper appears immediately below the main bulk of the northern prominence as seen on the limb. In the plane of the sky it appears to arch over lower lying prominence material observed in Hα, but projection effects make it difficult to determine the exact spatial relationship of the different features.

To obtain detailed thermal information and line-of-sight Doppler velocities, we placed the spectrograph slit of SUMER at a single location and took repeated exposures. The resulting data were then placed into a 2D context using data from *TRACE* and KSO. The general characteristics of the observations are given in Table 1.

### 2.1. SUMER

The SUMER (Wilhelm et al. 1995) data were collected from a single slit position off the limb shown relative to *TRACE* and Kanzelhöhe images in Figure 1. The slit was $1'' \times 120''$ illuminating
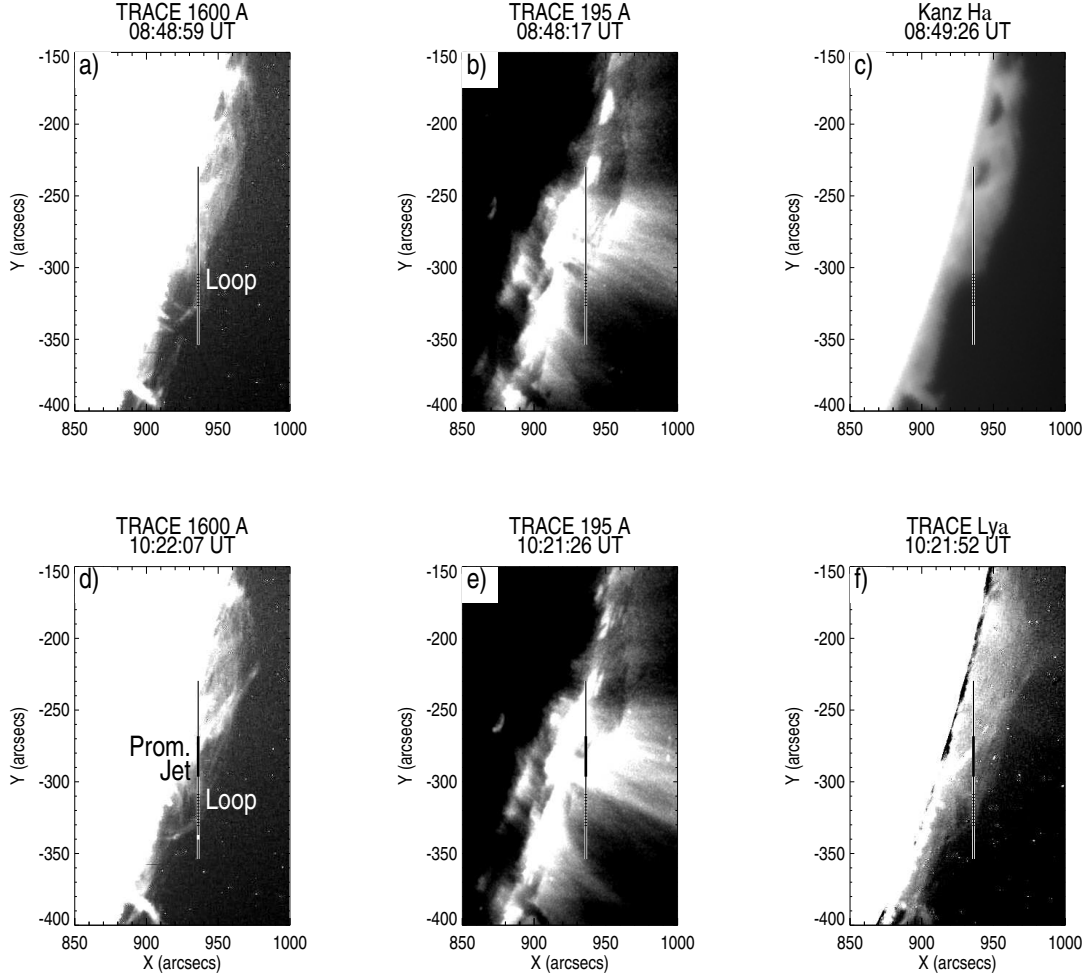
Fig. 1.— Context images from *TRACE* and Kanzelhöhe Solar Observatory. The SUMER slit position is shown by the line. The regions associated with the features discussed in §4.1 and 4.2 are labeled in panels (a) and (d). In panel (c) we label the approximate extents of the northern and southern prominences as seen near the limb. The top row shows images from ∼8:48 UT, while the bottom row shows images from ∼10:21 UT.

| Observatory | Times | Resolution | Cadence | Field of View |
|---|---|---|---|---|
| *SOHO*/SUMER | 6:00 -11:06 UT | $2''$ | 90 s | $1 \times 120''$ |
| *TRACE* | 6:00 -12:00 UT | $1''$ | 60-88 s | $512 \times 512''$ |
| Kanzelhöhe | 8:05-10:00 UT | $1.1''$ | 1 min | Full disk |
| | 11:15-12:40 UT | | | |

Table 1: Overview of Data Sets Used

the area vertically centered in the 1024×360 pixel detector, but the southernmost 12 pixels along the slit were unexposed. Data were collected with the B detector over the entire range from 747 to 793 Å, providing simultaneous profiles from lines in a temperature range from $\log T(\mathrm{K}) = 4.9$ - 6.2, as listed in Table 2. The lines also include O V lines that may be used as a density diagnostic (see § 3.4). Here we analyze data taken from 06:00-12:00 UT on 17 April 2003.

The SUMER data were corrected for local gain depression; there were not sufficient counts to require a dead-time correction. Frames were flat-fielded using the most recent B detector flat field, from Nov. 1998, shifted according to the method described by Carlsson, Judge & Wilhelm (1997), and each frame was corrected for distortion (Moran 2002). The radiometric correction of Feb. 2002 was applied. The radiometric calibration and thus our line intensity measurements have an estimated absolute uncertainty of 20%.

## 2.2. *TRACE*

In addition to the SUMER observations taken at a single location, we also obtained images with *TRACE* (Handy et al. 1999a) in the 1216, 1600, and 195 Å bands (see Table 3) with a cadence which was usually one image per 60-88 s. *TRACE* data were analyzed using the standard *TRACE* preparatory routines.

In order to obtain relatively pure maps of Lyα emission from the 1216 Å images, the 1600 Å band data were used to remove a long wavelength component which is present in the 1216 Å band (see Handy et al. 1999b). This technique, however, may not be completely adequate for analysis of moving features.

| Ion | Wavelength(s) (Å) | Peak Temperature (Log K) | Ion | Wavelength(s) (Å) | Peak Temperature (Log K) |
|-----|------------------|--------------------------|-----|------------------|--------------------------|
| N III | 764.34 | 4.9 | Ne VIII | 770.42 | 5.8 |
| N III | 763.33 | 4.9 | Mg VIII | 782.34 | 5.9 |
| N IV | 765.15 | 5.2 | Mg VIII | 762.65 | 5.9 |
| S V | 786.47 | 5.2 | S XI | 783.01 | 6.2 |
| O V | 760.43,760.21 | 5.4 | | | |
| O V | 761.13 | 5.4 | | | |
| O V | 761.99 | 5.4 | | | |

Table 2: *SOHO*/SUMER Lines Used

## 2.3. Kanzelhöhe Solar Observatory

Full disk H$\alpha$ data was available from Kanzelhöhe Solar Observatory from 08:05-12:40 UT, with a long gap from 10:00-11:15 UT due to problems with seeing.

## 2.4. Co-Registration

Comparisons between the SUMER N IV 765.15 Å and *TRACE* 1600 Å data indicate that the SUMER coordinates were offset from those of *TRACE* by (-4″,-32″). The *TRACE* coordinates lead to a more accurate fit of the solar limb, so the SUMER coordinates were adjusted accordingly. The alignment is good to about $\pm$ 1″.

*TRACE* and the Kanzelhöhe H$\alpha$ data were aligned by a comparison of the main prominence features observed in absorption in the 195 Å band images with those in emission in the H$\alpha$ data. The alignment is also accurate to about $\pm 1″$.

## 3. Data Analysis

### 3.1. Feature Selection

Figure 2 shows the SUMER N IV 765.16 Å line integrated intensity as a function of time and distance along the slit. Any moving change in intensity along the slit will appear as a diagonal line. We analyzed features in two different regions which are discussed in more detail below.

Most of the features were selected based on brightness and distinctness of the features from surrounding emission. This could lead to selection effects but seemed necessary for sufficient counting statistics to inspect subsections of each feature for evidence of changes as a function of time and distance along the feature trajectory. The two main areas we studied were the prominence,

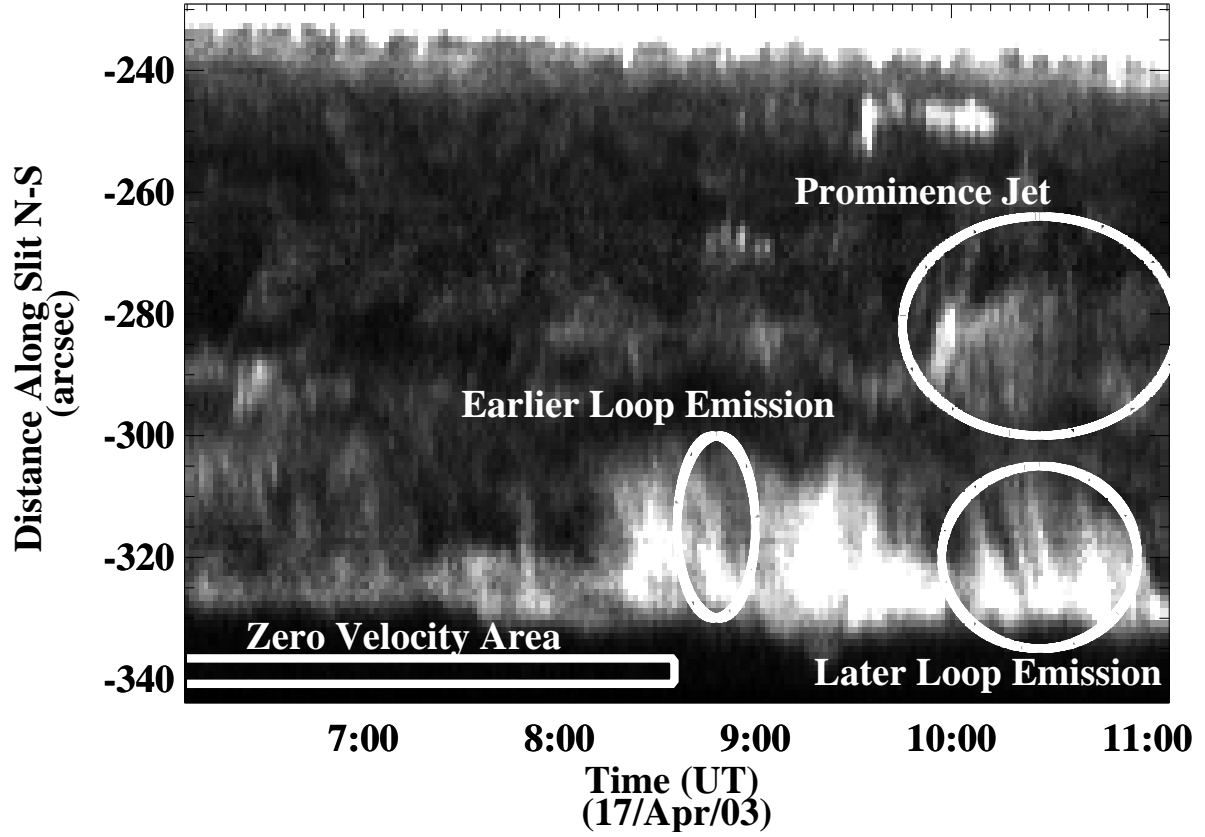| Wave-band (Å) | Sources of Emission | Temperature (Log K) |
|---|---|---|
| 1216 | Lyman $\alpha$ | 4.3 |
| 1600 | C IV | 5.0 |
| | Fe II, Si continuum | 3.6 − 4.0 |
| 195 | Fe XII | 6.2 |
| | H and He continuum absorption | 4.0 − 4.5 |
| | Fe XXIV | 7.3 |

Table 3: *TRACE* Wavebands

Fig. 2.— N IV 765.16 Å integrated intensity as a function of time and distance along the SUMER slit. The general times and locations of the features analyzed are shown, along with the region below the loop used for velocity calibration.

north of -300$''$, particularly a bright motion in the prominence starting at about 9:50 UT (§4.1), and motions in a loop observed between $y = -330$ and $-300''$ (§4.2). The features chosen show Doppler shifts relative to their surroundings, indicating that they are true mass motions.

## 3.2.    Background Selection

In order to isolate emission from the features of interest we must estimate background emission due to scattering in the instrument and also true emission in the background and foreground of the features of interest. The most accurate way to subtract the background emission from the transient sources is to use regions in the same spatial position as the features of interest but at different times when there was less emission. This method may lead to a misestimation of the background if the moving features were displacing emitting plasma present during the background interval rather than simply adding to it, or if significant time evolution were taking place. However, in general this method is more accurate than using a background taken from another location entirely.

We did experiment with using a background estimated using a region below the loop where there was very little emission with $\log T(\mathrm{K}) \lesssim 5.4$. This region did show significant emission for $\log T(\mathrm{K}) \gtrsim 5.8$, so in general it is not a reliable background estimate for higher temperature lines. Furthermore, because the area being studied was a plage region there were substantial spatial variations in the coronal temperature background. As a result, the use of this area below the loop to estimate background did have a substantial effect on DEM curves at $\log T(\mathrm{K}) \gtrsim 5.8$.

However, for $\log T(\mathrm{K}) \lesssim 5.4$ we found that using this alternate background led to changes in calculated quantities that were relatively small compared to our final order-of-magnitude estimates of their values. DEM values increased by factors of 2.6 and measured Doppler velocities changed by 2 to 6 km s$^{-1}$. Other quantities changed by factors of less than two: for instance, the maximum $n_e$ values increased by factors of 1.3 or less.

## 3.3.    Emission Measure

In order to determine the plasma DEM we used of the iterative procedure developed by Landi & Landini (1997). In this procedure, an arbitrary DEM curve $\varphi(T)$ is assumed as a starting point, and corrections to it are calculated by evaluating the ratio between observed intensities and theoretical values predicted using this initial curve; the corrected DEM is then assumed as the starting curve for the next iteration. Each line is associated with an effective temperature defined by

$$\log T_{\mathit{eff}} = \frac{\int \log T \; G(T)\varphi(T)dT}{\int G(T)\varphi(T)dT} \tag{1}$$

where $G(T)$ is the contribution function of each line. Contribution functions for all the observed lines have been calculated from CHIANTI 5.1 (Landi et al. 2006) under the ionization equilibrium assumption adopting the ion fractions of Mazzotta et al. (1998), and using the photospheric element abundances from Grevesse & Sauval (1998). The assumption of photospheric rather than coronal abundances makes no significant difference in the results for $\log T(\mathrm{K}) \leq 5.4$, but does affect DEMs at higher $T$, as is discussed in §4.1. Line emissivities have been calculated at a density of $3 \times 10^{10} \mathrm{cm}^{-3}$, the highest upper limit we measured. The lines used have little or no dependence on the electron density for densities lower than $10^{11} \mathrm{cm}^{-3}$, so our exact choice of density does not alter the determination of the DEM.

The DEM curve is generally defined between $\log T(\mathrm{K}) = 4$ and 8 K, but no lines are usually available to constrain the curve at the extremes of the temperature range, so it is customary to make assumptions on the value of the DEM at these extremes. In the present work, since we are dealing with non-flaring plasma, we assume that the DEM at $\log T(\mathrm{K}) = 8$ K is zero. The low-temperature point is more difficult to define. For the prominence jet there probably is material at $\log T(\mathrm{K}) = 4$ K. Unfortunately, we do not have radiometrically calibrated lines in our data set to constrain such cold plasma. In the present work, we have assumed that the DEM at $\log T(\mathrm{K}) = 4$ is zero. This assumption does not significantly affect the results at transition-region temperatures where N III lines are formed, because the contribution function of N III lines is negligible for $\log T(\mathrm{K}) < 4.4$. The other available ions are formed at even higher temperatures, so they are even less affected by cold plasma.

## 3.4. Density

The ratio of the O V line at 761.13 Å with either the 760.43,760.21 Å or the 761.99 Å O V lines provides an electron density diagnostic which is useful in the range $10^8 \lesssim n_e \lesssim 10^{12}$ cm$^{-3}$. The 761.13 Å line is relatively faint, and we found that we could only measure it for the initial source in the prominence jet (Feature A, see §4.1). In other cases we determined an upper limit to the line flux by measuring the intensity in a 0.7 Å band around the expected line location. This value was then compared with the integrated intensities of the other lines to calculate an upper limit to the possible electron density in the source. Even in the case in which we could measure the 761.13 Å line intensity, if the source is inhomogeneous, the diagnostic may not adequately reflect the actual electron densities present. However, the ratio should still provide a valid upper limit to the average $n_e$ because it would tend to represent the brighter, higher density areas.

We also derived a lower limit to the average density using integrals over the column DEM curves and estimates of source size along the line of sight. This value is a lower limit because we measure material only in the range $4.9 \lesssim \log T(\mathrm{K}) \lesssim 6.2$. Another consideration is that the observed line intensities could be reduced by Lyman absorption (Schmahl & Orrall 1986). This effect would reduce the DEM so our technique would still yield a valid lower limit.

## 3.5. Velocities

By combining the SUMER and *TRACE* data sets we are able to measure velocities both perpendicular to and along the line of sight.

To calibrate our line positions we assumed that the line position of the N IV line at 765.15 Å observed in featureless corona averages to zero. The background area south of the loop (see Fig. 2) is featureless in lines formed at $\log T(\mathrm{K}) < 5.4$. Because the features looked essentially identical (including plane of the sky speed) in all such lines we assume that these represent the same source with the same line-of-sight speed. The other lines were not used because the N III and O V lines were either too weak in this region or too blended to make a good wavelength calibration possible, and the S V 786.47 Å line was not completely Gaussian in low emission areas, perhaps indicating a blend with a coronal temperature line. In lines formed at higher temperatures ($> 500,000$ K) there were no suitable "empty" regions along the slit, so we did not measure absolute Doppler velocities with those lines.

## 3.6. Energy

With these velocity, density and volume estimates we calculate limits on the mass, the kinetic energy, pressure, and thermal energy of the features assuming an ideal gas composed solely of ionized hydrogen.

To calculate the pressure and thermal energy we use a weighted temperature determined using the DEM,

$$T_{avg} = \frac{\int T\varphi(T)dT}{\int \varphi(T)dT}. \tag{2}$$

Because there is very likely material below our cut-off, this is likely to be an overestimate. However, if material at lower temperatures were included the estimated minimum density, also derived from the DEM, would increase so that $P_{min} \propto T_{avg}n_{emin}$ would remain the same.

## 4. Results

## 4.1. Activated Prominence

### *4.1.1. Jet Velocity & Trajectory*

Starting at about 09:50 UT, a bright impulsive feature is seen in *TRACE* 1216 and 1600 Å moving upwards from the solar surface at an angle between 13 and 19° from the limb in the plane of the sky. The early stages of the jet are also visible in Hα before the Kanzelhöhe data was interrupted by clouds. With SUMER we see an initial burst of material moving across the slit

**N III 764.34 A**

**N IV 765.16 A**

**O V 760.43,760.21 A**

**S V 786.48 A**

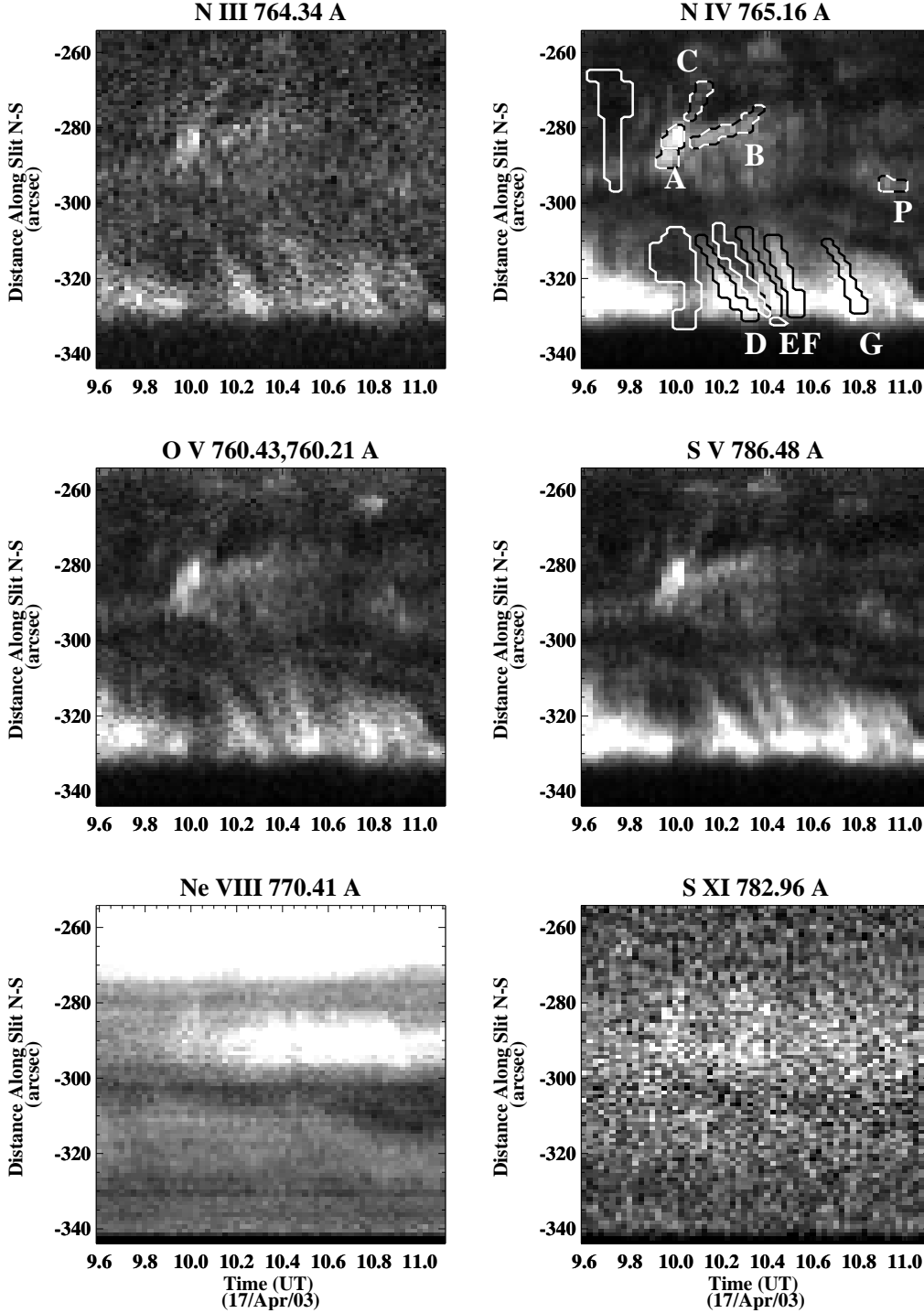**Ne VIII 770.41 A**

**S XI 782.96 A**

Fig. 3.— Integrated intensity of different lines as a function of time and distance along the slit from 10:00-11:00 UT. The top right panel outlines the features associated with the prominence jet, shown with dashed contours in Y = -200 to -260 (§4.1) and loop, outlined in black Y = -300 to -330″ (§4.2). The background areas are outlined in white.

(Feature A in Fig. 3), followed by a source that is the lower portions of the elongated feature moving northward (Feature B). In SUMER we also see another feature (C) which is not observed in the *TRACE* data, perhaps indicating that it lacks the cooler emission which contributes to the 1216 and 1600Å pass bands (see Table 3).

TRACE data show material falling down again starting around 10:44 UT and recrossing the SUMER slit at about 10:57 UT (Feature P). The overall duration of the event as seen in TRACE is about 80 minutes. This returning material follows a different path further from the solar limb than the upward moving feature. There is a fainter upwards motion along a similar trajectory starting around 11:15 UT, after the end of the SUMER observations. That material also starts to fall along a trajectory similar to that of the earlier feature when the *TRACE* observations end at 12:00 UT. H$\alpha$ data covering the time of this second, smaller motion also show upwards moving material.

On the upwards portion of the motion, speeds in the plane of the sky measured from *TRACE* data range from 42 - 52 km s$^{-1}$ for the leading edge of the upwards motion to 25 km s$^{-1}$ for the trailing portion of the feature. Speeds for the downwards portion of the motion are about 55 km s$^{-1}$. Similar speeds characterize the motion starting at 11:15 UT.

SUMER data show redshifted velocities of about 32 km s$^{-1}$ for Features A and B, and 22 km s$^{-1}$ for Feature C. The returning feature, P, also shows a redshift of about 9 km s$^{-1}$.

The redshift of the downward moving feature further confirms that it is not returning to the original location, but is moving both back towards the limb and continuing away from the viewer on another path. Thus it seems that the plasma is moving up and then down an inclined loop-like structure with a length in the plane of the sky of about 160 Mm.

### 4.1.2. Jet Thermal Properties

The sources associated with the jet are clear in all SUMER lines formed at $T < 250,000$ K, with some signs of emission at higher temperatures.

We note that although the jet and the moving features in the active loop discussed below (§4.2) seem to be of comparable intensity in the SUMER data from lines produced at $\log T(\mathrm{K}) \approx 5$, in the *TRACE* 1216 and 1600 Å bands the emission from the prominence jet is far brighter. This suggests that the cooler emission from Fe II and the Si continuum in the 1600 Å makes a substantial off-limb contribution in the prominence, while the C IV emission at $\log T(\mathrm{K}) = 5$ is the main emission present in the loop discussed in §4.2.

There does not seem to be any associated emission in the *TRACE* 195 Å band, which has a very strong contribution from Fe XII at 1.5 MK. Rather, those data show chiefly the motion of cooler absorbing material in areas corresponding to the bright jet material seen in the 1216 and 1600 Å bands.
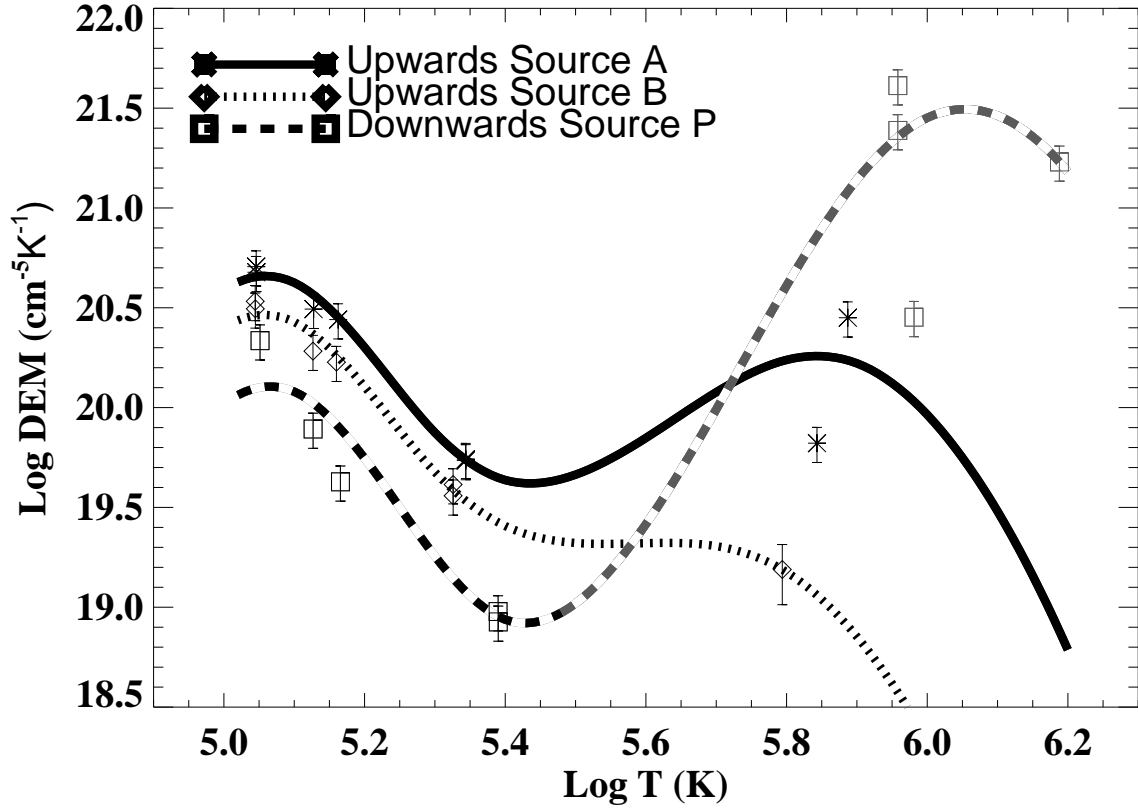
Fig. 4.— Column DEM curves for portions of the prominence jet. These curves all show a similar shape for $\log T(\mathrm{K}) \lesssim 5.4$. The high amount of hot plasma shown for Source P (shown with a lighter grey curve) may be due to problems in correctly estimating the background emission.

Shown in Figure 4 are DEM curves derived from the observations of the jet at different times: the initial motion (A), the base of the feature as it moved northwards along the slit (B), and as the material fell downwards again (P).

For $\log T(\mathrm{K}) \leq 5.4$ the DEM curves all show the same shape within the error bars. There is substantial variation in the DEMs of the hotter material, with the initial source (A) showing more Ne VIII emission than the second source (B).

The falling source (P) appears to show a substantial hot component, but this apparently high amount of coronal temperature emission may be due to problems in correctly estimating the background emission, which was derived from data taken over an hour before the appearance of Feature P. The portion of the curve for $\log T(\mathrm{K}) \gtrsim 6$ is entirely based on a single rather faint S XI line. The S XI data in Figure 3 combined with the lack of an associated source in the *TRACE* data from Fe XII suggest that the apparent $\log T(\mathrm{K}) = 6$ component may just be due to a change in the background between the times of the background area and the source.

The Mg VIII lines predict more material at $\log T(\mathrm{K}) = 5.8$ than does the Ne VIII line by a factor of $\approx 6$ for Feature A and ten for Feature P. This discrepancy would be substantially resolved if coronal rather than photospheric abundances were assumed in the DEM calculation. This suggests that either the jet material does have coronal abundances or that the Ne VIII and Mg VIII emission is actually hot background material being revealed by the motion of cooler absorbing foreground material. Without contemporaneous 2D imaging it is hard to tell. As mentioned above Feature P may be contaminated with some incompletely subtracted coronal emission. However, because the shape of Feature A is very similar in the Ne VIII and the cooler lines we think that the $\log T(\mathrm{K}) \approx 5.8$ emission in Feature A is indeed from the moving source.

A source observed in SUMER Ne VIII and Mg VIII near the southern extent of the jet ($\approx -290''$) persists for at least 50 min, until the end of the observations. In Ne VIII it appears as a series of four brightenings. The *TRACE* 195 Å data, which show both cool emission and 1.5 MK plasma are a bit sparse during this time but suggest the variations are likely to be due to dark absorbing material moving across a brighter background source.

### 4.1.3. Dimensions of Prominence Jet

Feature A seems to move through the SUMER slit in its entirety without greatly changing dimensions. This may not be the case for the other sources, which are more difficult to characterize. The SUMER data for Feature B probably shows the base of much longer feature lying across the slit and moving northward as a whole. The edges of the falling material corresponding to Feature P are not easily definable from the *TRACE* data. As a result, it is not clear that the density estimates based on SUMER data should be applied to any jet feature other than Feature A. For other features the density might not apply to all the material seen in *TRACE*, and it is not clear what volume would be the correct one to use for further calculations. Therefore we have only

attempted to calculate further physical parameters for Feature A.

Based on the *TRACE* images the source length of Feature A in the plane of the sky is about 14 Mm. We correct this for projection effects using the angle calculated from the velocities in the plane of the sky and along the line of sight, which indicate an angle from the plane of the sky of $32 \deg \pm 7 \deg$. We assume the source is roughly cylindrical with this value as a length and with a diameter equal to the sources' width in the plane of the sky, about 7 Mm.

We use these dimensions and the other parameters derived from SUMER and *TRACE* to characterize Feature A, as presented in Table 4. We note that the density minimum in this case is likely to be a substantial underestimate because the source clearly emits in Ly$\alpha$ and probably in H$\alpha$, both produced at temperatures substantially below the limit of the DEM calculation upon which the density lower limit is based.

## 4.2. Dynamic Loop

In Figure 3 repeated motions can be seen in the lines with $T \lesssim 250,000$ K in the region between -300 and -330″. We designated four of these features occurring between 10:00 and 11:00 UT as Features D-G. These features are in the same location and have approximately the same speed. The features were chosen because they were distinct and easily separable, although we also analyzed a less easily separable feature (Feature H) observed at an earlier time when H$\alpha$ data was obtained. Features appeared in the SUMER data for 7 to 14 minutes, but some features could be traced in the 2-D *TRACE* movies for as long as 25 minutes.

The 1600 and 1216 Å band *TRACE* and Kanzelhöhe H$\alpha$ images (Fig. 1) reveal that these repeated motions are in a loop south of the main bulk of the prominence. The exact geometry of the loop is difficult to determine because of projection effects. The loop appears somewhat elongated, and the angle calculations given below suggest that this is even more the case when projection effects are taken into account. In the plane of the sky the loop is situated above low-lying H$\alpha$ emission that is probably part of one of the prominences. The northern footpoint extends to the latitude of the bulk of the northern prominence, making it difficult to see. The southern foot point is south of the main portion of that prominence as seen on the limb. Motions along the loop go from north to south. If it is assumed that the loop extends down to the solar surface, then its length is $\approx$70,000 km in the plane of the sky and height is $\approx$24,000 km. There is some indication from the *TRACE* data that the material is flowing along the northern portion of the loop before it passes the SUMER slit near the top of the loop and falls downward along the southern leg.

The loop containing these features was apparent in the *TRACE* data starting at about 8:30 UT through the end of the *TRACE* observations at 12:00 UT. Another loop nearby (in the plane of the sky) was visible as early as 6:00 UT, but the southern footpoint of that loop has a slightly different location. The loop height varied over the period of observation so that the loop does not always cross the area covered by the SUMER slit. However, emission in the area of the loop can be seen
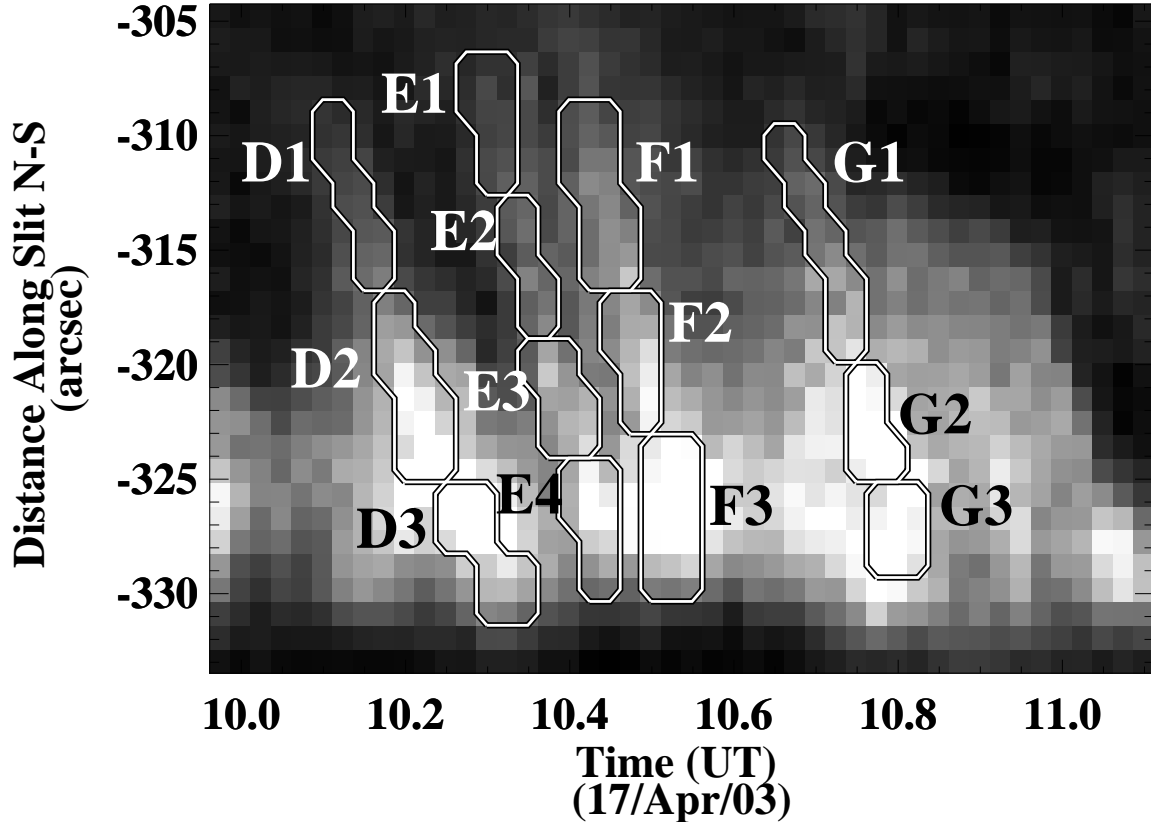
Fig. 5.— Sub-Features of Features D-G. The gray scale image is N IV 765.16 Å integrated intensity as a function of time and distance along the SUMER slit. Each Sub-feature isolates emission from a different location, and thus time, along the trajectory of a moving feature.

in lines formed at $T \lesssim 250,000$ K for most of the observing period after 8:30 UT.

The combined observations indicate that the moving loop features chiefly contain plasma in the temperature range $20,000 \lesssim T \lesssim 250,000$ K.

Lines formed at $\log T(\mathrm{K}) \approx 5.8$, especially Ne VIII, show emission in this area, but it does not vary greatly in time or show the moving features seen at lower temperatures. This suggests that the $\log T(\mathrm{K}) \approx 5.8$ emission is due to either other features in the background or foreground or perhaps to diffuse emission from the loop. There is no sign of loop emission for $\log T(\mathrm{K}) > 6$ in the *TRACE* 195 Å data.

The features do not show evidence of emission at $\log T(\mathrm{K}) \approx 4$. No Hα data was taken at the time of Feature D-G. However at earlier and later times the Hα data do not show material at the position of the loop, although they do show loops beneath it, closer to the limb. After 11:00 UT there is some indication of Hα emission along the northern part of the loop, but no evidence of moving features. The *TRACE* 195 Å band confirms this lack of low temperature material, showing no absorption at the location of the loop. The loop can be seen in Lyα although the moving features are faint. The Hα and Lyα data are not radiometrically calibrated so they cannot give us a quantifiable limit to the amount of cool material, but the observations do suggest that there is little material as compared to the prominence at $T \lesssim 30,000$, the temperature of the He$^+$ Lyman absorption probably responsible for features seen in the *TRACE* 195 Å band.

We also analyzed a feature observed at 8:45 UT (see the "Earlier Loop Emission" in Fig. 2), a time when Hα data also were available. At this time moving UV emission was visible in the loop, but the discrete moving sources were harder to identify. There was no Hα emission from the features. We choose this feature (Feature H) to establish the DEM of a feature during a time when we could demonstrate that there was not significant Hα emission from the feature. The DEM of Feature H did not differ significantly from those of Features D-G (see next section).

### 4.2.1. Loop DEMs

DEM curves were calculated for two to four sub-features in each of the main features (D, E, F, G, & H) studied. The sub-features, shown in Figure 3, represent the moving features at different times and locations along their trajectories. We found that sub-features in the southern part of Feature G and in parts of Feature H had clear non-Gaussian components. These could not be removed via background subtraction, and we did not use these in our analyses.

Typical column DEM(T) values for these sources are shown in Figure 6. As described in §4.2.1 we assumed that there was no emission below $\log T(\mathrm{K}) = 4$ or above $\log T(\mathrm{K}) = 8$. The former assumption is justified by the lack of Lyman absorption and also the lack of Hα emission associated with Feature H.

Although Ne VIII emission from the general location of the loop is clearly observed, there are
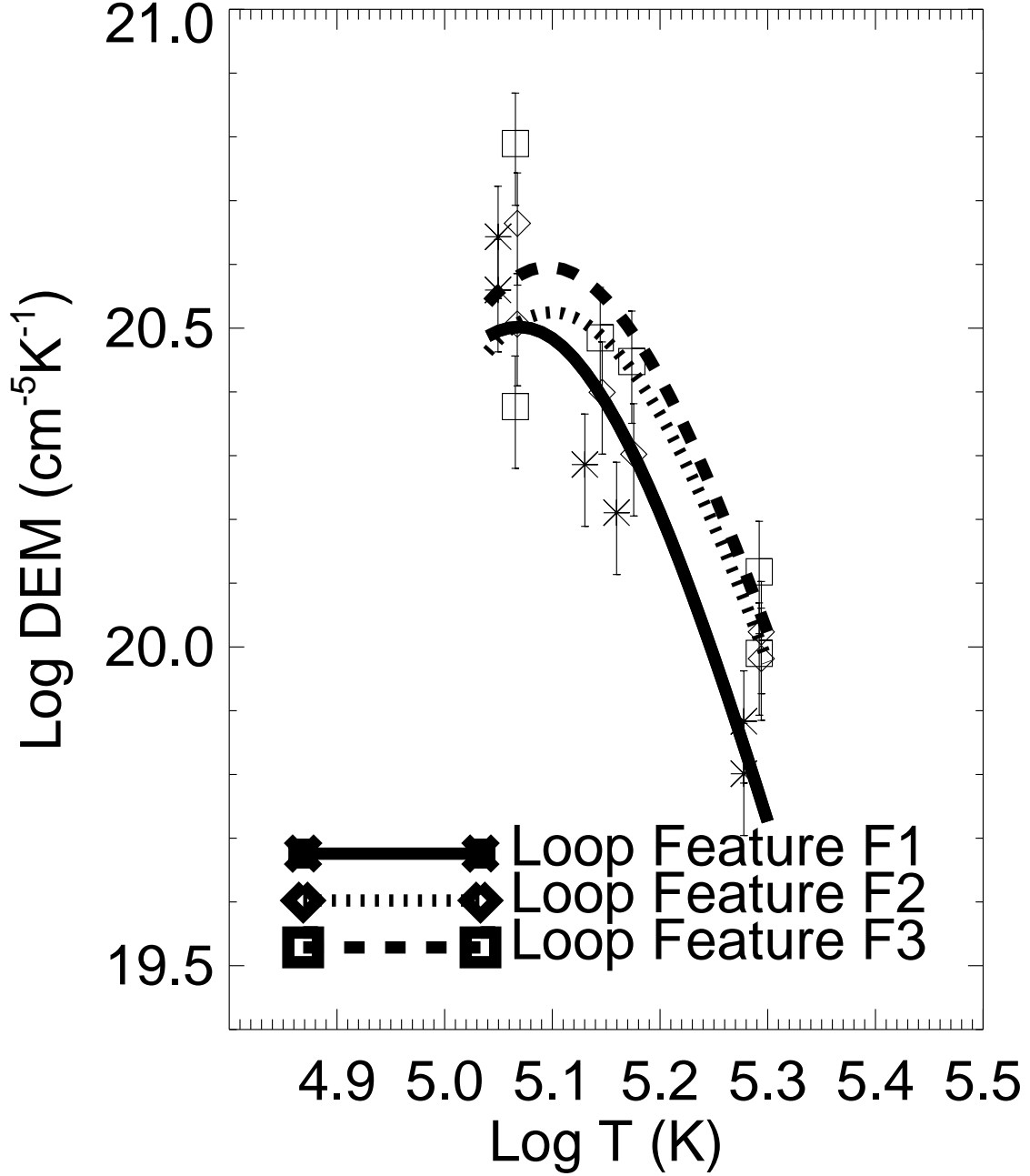
Fig. 6.— Column DEM curves for Feature F, one of the moving features in the loop. The three different curves show the feature at different times and thus locations along the loop. The subfeatures are marked in Fig. 5. Within the uncertainties shown by the error bars, the shapes of the curves are the same. This is true for 14 of the 15 loop sub-feature DEM curves.

no signs of the moving sources in the Ne VIII emission or in the Mg VIII or S XI lines. Emission from lines produced at $\log T(\mathrm{K}) \gtrsim 5.8$ is removed by the background subtraction.

The DEM values indicate that, to within the uncertainties of our calculation, the shapes of the thermal distributions do not change either in a given feature as a function of time or between the features. The data show a decrease of material from $\log T(\mathrm{K})=4.9$ (N III) through $\log T(\mathrm{K})=5.4$ (O V). There was only one exception to this: the DEM curve for the earliest and northernmost sub-feature in Feature D showed a significantly flatter slope after background subtraction than other DEM curves.

We found no evidence for timing differences in the features at different temperatures, i.e., the emission from the sources appears to be co-temporal and co-spatial in the different lines in which they were observed.

### 4.2.2. Loop Velocity & Trajectory

The *TRACE* data indicate that the SUMER slit is located along the top of the loop. SUMER Doppler measurements reveal blue-ward shifts of 17 to 31 km s$^{-1}$, while speeds in the plane of the sky vary from 16 to 30 km s$^{-1}$. These velocity components allow us to measure the direction of motion and thus the orientation of the loop top. We find angles from the line of sight ranging from 29-52°, indicating that the loop is roughly aligned with the filament channel. It is possible that the loop is crossing some portion of the channel, although we cannot say for sure.

There are variations of 10 to 25 km s$^{-1}$ in the Doppler velocities measured in the different sub-features of a given feature. In most cases these sub-feature velocity variations are consistent in both the N IV and S V lines. However, there was no evidence that the features systematically speed up or slow down as they move along the loop. The relative one $\sigma$ uncertainties on the velocities based on the line fits is 0.8 to 2 km s$^{-1}$.

### 4.2.3. Dimensions of Loop Features

The estimated density, velocity, mass, pressure, energy, and source sizes for Feature D-G are presented in Table 5.

Based on the *TRACE* observations the average feature length in the plane of the sky is $5.4 \pm 0.9$ Mm. This length is about 8% of the loop length in the plane of the sky. As with the prominence jet, we model the feature as a cylinder whose the length is that measured with TRACE corrected for foreshortening and the diameter is the source width also measured with TRACE. The same plane-of-sky dimensions are used as a starting point for all of Features D-G, although the foreshortening correction depends on the Doppler velocity measured for each source.

| Feature | A |
|---|---|
| v (km s$^{-1}$) | $38 \pm 4$ |
| Min $n_{eavg}$ (cm$^{-3}$) | $(1 \pm 0.3) \times 10^8$ |
| Max $n_{eavg}$ (cm$^{-3}$) | $(3 \pm 0.3) \times 10^9$ |
| Min Mass (g) | $(2 \pm 1.6) \times 10^{11}$ |
| Max Mass (g) | $(6 \pm 3.6) \times 10^{12}$ |
| Min Kinetic Energy (ergs) | $(2 \pm 1.2) \times 10^{24}$ |
| Max Kinetic Energy (ergs) | $(4 \pm 2.8) \times 10^{25}$ |
| Min Pressure (dyne cm$^{-2}$) | $(2 \pm 0.1) \times 10^{-2}$ |
| Max Pressure (dyne cm$^{-2}$) | $(4 \pm 0.2) \times 10^{-1}$ |
| Min Thermal Energy (ergs) | $(2 \pm 1.5) \times 10^{25}$ |
| Max Thermal Energy (ergs) | $(6 \pm 3.6) \times 10^{26}$ |
| Min Filling Factor | $(4 \pm 0.9) \times 10^{-2}$ |
| Length (Mm) | $28 \pm 9$ |
| Diameter (Mm) | $7 \pm 2$ |
| Repeat Time (min) | 85 |

Table 4: Physical Parameters calculated for Feature A. The Repeat Time is the time between this jet and a latter motion occurring along the same trajectory.

| Feature | D | E | F | G |
|---|---|---|---|---|
| Time (UT) | 10:07 | 10:21 | 10:25 | 10:40 |
| v (km s$^{-1}$) | $35 \pm 4$ | $40 \pm 4$ | $37 \pm 4$ | $26 \pm 4$ |
| Min $n_{eavg}$ (cm$^{-3}$) | $(3 \pm 0.5) \times 10^8$ | $(2 \pm 0.4) \times 10^8$ | $(3 \pm 0.6) \times 10^8$ | $(4 \pm 0.7) \times 10^8$ |
| Max $n_{eavg}$ (cm$^{-3}$) | $(4 \pm 0.3) \times 10^9$ | $(8 \pm 0.5) \times 10^9$ | $(9 \pm 0.4) \times 10^9$ | $(9 \pm 0.5) \times 10^9$ |
| Min Mass (g) | $(2 \pm 1.4) \times 10^{10}$ | $(2 \pm 0.9) \times 10^{10}$ | $(2 \pm 1.0) \times 10^{10}$ | $(2 \pm 1.2) \times 10^{10}$ |
| Max Mass (g) | $(4 \pm 2.2) \times 10^{11}$ | $(6 \pm 3.0) \times 10^{11}$ | $(5 \pm 2.7) \times 10^{11}$ | $(5 \pm 2.6) \times 10^{11}$ |
| Min Kinetic Energy (ergs) | $(1 \pm 0.9) \times 10^{23}$ | $(1 \pm 0.7) \times 10^{23}$ | $(1 \pm 0.8) \times 10^{23}$ | $(8 \pm 5.1) \times 10^{22}$ |
| Max Kinetic Energy (ergs) | $(2 \pm 1.5) \times 10^{24}$ | $(5 \pm 2.6) \times 10^{24}$ | $(4 \pm 2.0) \times 10^{24}$ | $(2 \pm 1.1) \times 10^{24}$ |
| Min Pressure (dyne cm$^{-2}$) | $(1 \pm 0.1) \times 10^{-2}$ | $(9 \pm 0.8) \times 10^{-3}$ | $(1 \pm 0.1) \times 10^{-2}$ | $(2 \pm 0.1) \times 10^{-2}$ |
| Max Pressure (dyne cm$^{-2}$) | $(2 \pm 0.1) \times 10^{-1}$ | $(3 \pm 0.1) \times 10^{-1}$ | $(4 \pm 0.1) \times 10^{-1}$ | $(3 \pm 0.1) \times 10^{-1}$ |
| Min Thermal Energy (ergs) | $(8 \pm 4.6) \times 10^{23}$ | $(6 \pm 3.1) \times 10^{23}$ | $(7 \pm 3.5) \times 10^{23}$ | $(8 \pm 4.2) \times 10^{23}$ |
| Max Thermal Energy (ergs) | $(1 \pm 0.7) \times 10^{25}$ | $(2 \pm 1.1) \times 10^{25}$ | $(2 \pm 1.0) \times 10^{25}$ | $(2 \pm 0.9) \times 10^{25}$ |
| Min Filling Factor | $(6 \pm 1.3) \times 10^{-2}$ | $(3 \pm 0.5) \times 10^{-2}$ | $(4 \pm 0.6) \times 10^{-2}$ | $(5 \pm 0.8) \times 10^{-2}$ |
| Length (Mm) | $11 \pm 3$ | $9 \pm 2$ | $7 \pm 1$ | $7 \pm 2$ |
| Diameter (Mm) | $2.5 \pm 0.6$ | | | |
| Repeat Time (min) | 4-15 | | | |

Table 5: Physical parameters for features observed in the loop. The Time is when the peak of the feature crossed Y=-310$''$. The Repeat Time is the time between successive motions.

These sources were selected because they were relatively discrete and hence easily separable from one another. The more complicated emission from the sources at earlier times (e.g., 8:40 UT in Fig. 2), may not be well represented by sources of this size.

## 5.    Discussion

### 5.1.    Emission Measure

Typical DEM curves in the solar atmosphere exhibit a minimum at $\sim 10^5$ K with increases at either side. Prominence DEMs also show this characteristic, although the higher temperature portion of the curve is presumed to be chiefly unsubtracted emission from the surrounding corona. This shape can be seen in Fig. 7 which shows DEM curves from previous measurements of a prominence and background corona (Cirigliano, Vial & Rovira 2004) and an active region Brosius et al. (2000) and compared to DEMs from the jet and loop studied in this paper.

There have only been a few DEM analyses of prominences. Engvold (1988) present EM curves measured with ATM/Skylab which show minima around $\log T(\mathrm{K}) \approx 5.1$. Schmahl & Orrall (1986) present prominence DEM curves showing a similar structure with roughly $T^{-2}$ dependence in the range $4.8 < \log T(\mathrm{K}) < 5.0$. They also note a strong suppression of prominence emission observed in lines below the Lyman cut-off at 912 Å compared with lines above, presumably due to Lyman absorption by the cool prominence. More recently, Cirigliano, Vial & Rovira (2004) used SUMER and CDS to determine a prominence DEM curve (Fig. 7). They also found a curve with a minimum near $\log T(\mathrm{K}) \approx 5.2$ a rough power law dependence with an index slightly below $-2$ in the range $4.8 < \log T(\mathrm{K}) < 5.2$.

Observational active-region DEM curves calculated by Brosius et al. (1996, 2000) and Schmelz et al. (1999) have higher temperature minima, $\log T(\mathrm{K}) \approx 5.7$ (see Fig.7), and can be fit with a slightly higher power law index ($\approx -2.8 \pm 0.2$ for $5.0 < \log T(\mathrm{K}) < 5.5$).

Our work differs from these earlier studies in two ways. We are emphasizing the study of relatively small moving features. Most previous measurements have been of much larger regions of the prominence or active region or even combined observations of more than one object (e.g., Engvold 1988). We also attempted to remove coronal background emission, although in some cases (e.g., Feature P, the falling activated material) it probably still remains to some extent.

We find the typical decreasing curve for transition-region temperatures, although our curves are consistent with a power law index of $\approx -3$ making them steeper in the range $4.8 < \log T(\mathrm{K}) < 5.5$ than any of those shown in the sources cited above, including the prominence and active region curves. This difference does not seem to be due to the background subtraction.

The background subtraction is responsible for the lack of a "coronal" temperature component in the DEM of the moving loop features. We still find some component at $\log T(\mathrm{K}) > 5.5$ in the jet
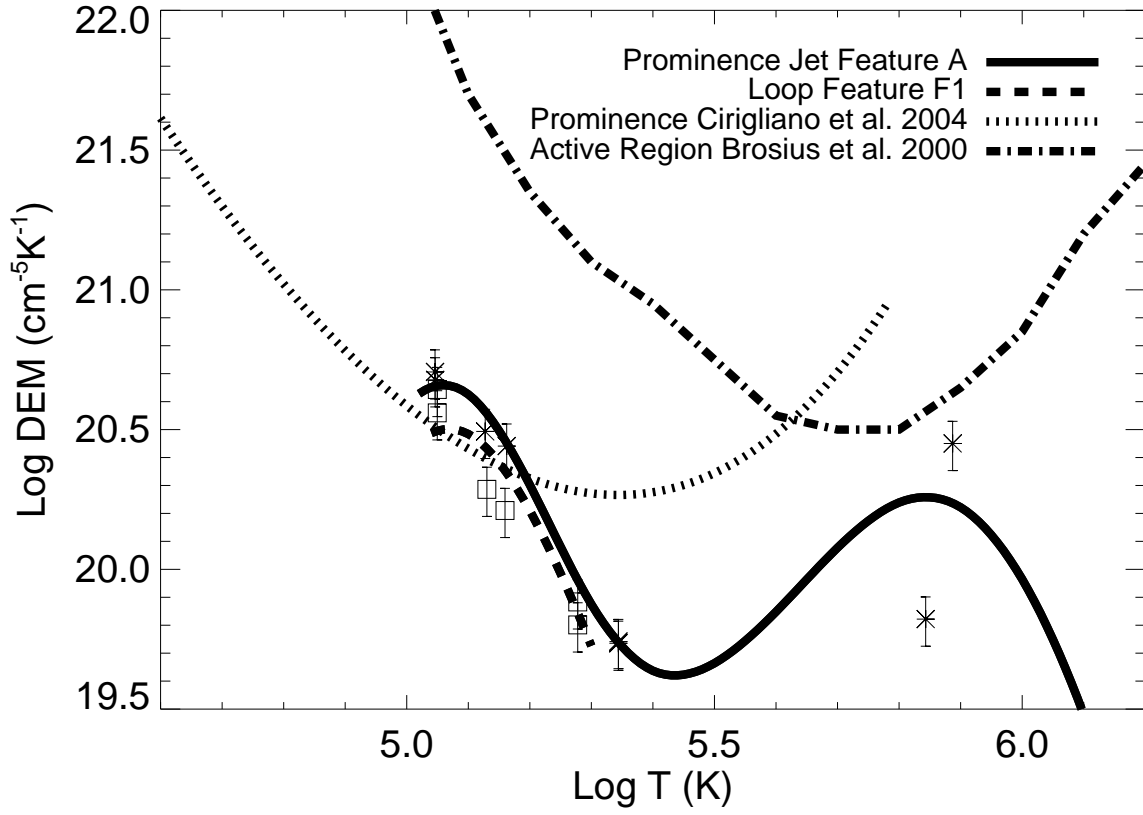
Fig. 7.— Column DEM curves from the jet and loop studied in this paper compared to data from Brosius et al. (2000) and a curve based on points measured from the plot of the DEM of a prominence plus corona in Cirigliano, Vial & Rovira (2004)

even after background subtraction. Because background subtraction makes such a great difference for $\log T(\mathrm{K}) > 5.5$ it is not meaningful for us to compare our DEM results in this range with curves for which no background subtraction was done.

## 5.2. Prominence Jet

General measurements of densities in prominences span a wide range from $10^9 - 10^{12}$ cm$^{-3}$, as compared to our estimate of $1 \times 10^8 < n_e < 3 \times 10^9$ cm$^{-3}$. The quickly moving features representing prominence activation are often in the low end of this range, e.g, $2 \times 10^9$ cm$^{-3}$ for an activation in a prominence observed by Stellmacher, Koutchmy, & Lebecq (1986) or $(0.7 - 1.9) \times 10^{10}$ cm$^{-3}$ for jets in prominences observed with *TRACE* by Chae (2003).

The jet we discuss in this paper is about 3-85 times less massive than those described by Chae (2003). Another distinction between this feature and those described by Chae is that this jet is probably subsonic and does not have greatly more kinetic than thermal energy per particle.

Our DEM suggests a more complicated temperature structure than that found by Chae. Using a *TRACE* three-filter method he found that the jets and eruptions studied were probably isothermal with a temperature in the range $5.3 < \log T(\mathrm{K}) < 5.48$. For the jet studied here, the DEM derived from SUMER spectral data indicates a multithermal structure, with plasma at least as low as $\log T(\mathrm{K}) = 5.0$ and probably as high as 5.8 with a minimum near 5.45. Although this difference may be due to the fact that we are analyzing different events, another important factor is probably the superior temperature discrimination of the SUMER spectrometer over that of a broad-band imager.

**Reconnection Driven Jets** A commonly cited model for prominences in general and jets in particular invokes upward plasma motion propelled by magnetic field reconnection in the chromosphere or photosphere at prominence footpoints. This idea has been put forth by observers of fast activation motions seen in H$\alpha$ and the UV (e.g., Wang 1999; Chae et al. 2000a), who often find correlations between flux cancellation and jets. Developing the model further, Litvinenko & Martin (1999) analyzed a particular flux cancellation event and calculated a possible mass flux from this mechanism of $1.1 \times 10^{12}$ g s$^{-1}$, which would be quite sufficient for the source studied here. The mechanism can propel the mass at velocities at a few tens of km s$^{-1}$, also consistent with our observations. The thermal aspects of this model have not been developed, however, so it is not clear what should be expected as far as a temperature distribution.

## 5.3. Nature of the Loop

The loop is aligned in roughly the direction of the lower bend in the "S" observed in the northern prominence as it appeared earlier against the disk. This suggests that the loop may be a sheared loop crossing the northern prominence channel. Such a loop might be a transition between the arcade loops perpendicular to the prominence and sheared prominence field lines which figure in, e.g., the sheared arcade model of DeVore & Antiochos (2000).

The loop does not resemble one of the loops studied by Schrijver (2001) with *TRACE*. Those loops appeared initially at coronal temperatures and then showed draining cool material. Although there were coronal temperature loops in the vicinity of the loop studied in this paper, we find no evidence that the motions observed are connected to any coronal temperature structure.

In addition to the lack of coronal temperature emission associated with the moving loop features, no H$\alpha$ emission appears to be produced by these features. These observations present a puzzle. In general it should be very hard to sustain a plasma with $\log T(\mathrm{K}) \approx 5$ unless it is cooling from a higher temperature or serving as the interface between the hot corona and a cooler chromospheric-temperature plasma. It is, of course, possible that there is some cooler material associated with this loop but not enough to be discernible in H$\alpha$ or in absorption in the *TRACE* 195 Å band. It would be helpful in this case to be able to combine radiometrically calibrated H$\alpha$ and UV data.

**Flux tube heating models**   This investigation provides a set of parameters for comparison with models of solar loop dynamics. One variety of these models are ones in which heating, usually asymmetric and at or near loop foot points results in upward moving flows. Hot flows may cool and condense, forming features that move under the influence of gravity or because of pressure differentials in the loop. There are many models of this type and, depending on the physical parameters, these have been applied to both motions in prominences (e.g., Antiochos et al. 2000; Karpen et al. 2001) and in loops, usually coronal, although a few models investigate material with $\log T(\mathrm{K}) < 6$ (e.g., Spadaro et al. 2003; Gudiksen & Norlund 2005; Gontikakis et al. 2005).

Perhaps the greatest challenge to these models presented by these data is the quick repetition rate of the moving sources in the cool loop. Although the general loop structure seems to remain for hours, the time between features is as small as 5 minutes in the loop. The cycle times in many of the models thus far have been much longer: for instance, hours for studies of prominence flux tubes (220 Mm) done by Karpen et al. (2001, 2005), 1-2 hours in the case of shorter coronal (10 Mm) loops modeled by Müller, Hansteen, & Peter (2003).

Repeat times on the order of a few minutes may be achievable with a time varying energy input. In studies of coronal loops exhibiting runaway cooling, Mendoza-Briceño et al. (2005) found that random impulsive heating on time scales of a few minutes can produce cool features to appear at intervals of 3 to 10 minutes in loops of length 5 to 30 Mm. This may not apply directly to our

observations, as we do not appear to be observing a cooling and draining coronal loop, but the time scales are promising.

It is possible that the motions are occurring along adjacent but separate field lines in the same general structure. This would mean that the process was not actually repeating at the same time scale along the same field line.

## 6. Summary

We have analyzed moving features seen in a prominence jet and a nearby "transition region" temperature loop, and have determined sizes, intervals of repetition, velocities and trajectories, and limits to kinetic and thermal energies associated with the motions.

The loop does not seem to have a coronal component, indicating that it is not a specimen of the cooling loops described by Schrijver (2001) or modelled by Mendoza-Briceño et al. (2005). Instead it appears to be a relatively long (over 70 Mm), long-lived (hours) stretched loop aligned roughly in the direction of the prominence channel. The moving features are approximately 8% of the loop length and appear to be mostly confined to a temperature range $4.4 \lesssim \log T(\mathrm{K}) \lesssim 5.4$. We suggest that the loop may be part of a sheared, low-altitude arcade-like structure spanning the prominence channel. The motions repeat at intervals as low as five minutes. Loop modeling efforts to this point suggest that this rapid rate may require a time varying energy input.

The motion in the prominence is a lower-energy example of jets seen by observers such as Chae (2003) with *TRACE*. We are able to trace the trajectory of the jet feature as it moves upwards and then moves downwards again further along the prominence. The spectrum based DEM analysis reveals that the jet is a multithermal structure with plasma at least as low as $\log T(\mathrm{K}) = 5.0$ and probably as high as $\log T(\mathrm{K}) = 5.8$. Reconnection-jet models of similar upward motions are capable of accelerating the observed masses, but have not been extended to model thermal aspects of these phenomena such as we measure here.

*Facilities:* SOHO (SUMER), TRACE, Kanzelhöhe

## REFERENCES

Antiochos, S. K., MacNeice, P. J., & Spicer, D. S. 2000, ApJ, 536, 494

Brekke, P., Kjeldseth-Moe, O., Brynildsen, N., Maltby, P., Haugan, S.V. H, Harrison, R.A., Thompson, W.T., & Pike, C.D. 1997, Sol. Phys., 170, 163.

Brosius, J.W., Davila, J.M., Thomas, R.J., & Monsignori-Fossi, B.C. 1996, ApJS, 106, 143

Brosius, J. W., Thomas, R.J., Davila, J.M., & Landi, E. 2000, ApJ, 543, 1016

Carlsson, M., Judge P.G., & Wilhelm K. 1997, ApJ, 486, L63

Chae, J. 2003, ApJ, 584, 1084

Chae, J., Denker, C., Spirock, T. J., Wang, H., & Goode, P. R. 2000a, Sol. Phys., 195, 333

Chae, J., Wang, H., Qiu, J., Goode, P.R., & Wilhelm, K. 2000b, ApJ, 533, 535

Cirigliano, D., Vial, J.-C., & Rovira, M. 2004, Sol. Phys., 223, 95

DeVore, C.R. & Antiochos, S.K. 2000, ApJ, 539, 954

Di Giorgio, S., Reale, F., & Peres, G. 2003, A&A, 406, 323

Engvold, O, 1988, Solar and stellar coronal structure and dynamics; Proceedings of the Ninth Sacramento Peak Summer Symposium, Sunspot, NM, Aug. 17-21, 1987. Sunspot, NM, National Solar Observatory, 1988, p. 151

Fredvik, T., Kjeldseth-Moe, O., Haugan, S. V. H., Brekke, P., Gurman, J. B., Wilhelm, K 2002, AdSpR 30 635

Gontikakis, C., Petrie, G.J.D., Dara, H.C., Tsinganos, K. 2005 A&A, 434, 1155

Grevesse N., & Sauval, A.J. 1998, Space Sci. Rev., 85, 161

Gudiksen, B.V. & Norlund, Å. 2005 ApJ, 618, 1031.

Handy, B.,N., Acton, L.W. Kankelborg, C.C., et al. 1999a, Sol. Phys.187 229

Handy, B.,N., Tarbell, T.D., Wolfson, C.J., Korendyke, C.M., & Vourlidas, A. 1999b, Sol. Phys., 190, 351

Karpen, J.T., Antiochos, S.K., Hohensee, M., Klimchuk, J.A., & MacNeice, P.J. 2001, ApJ, 553, L85

Karpen, J.T., Tanner, S.E.M., Antiochos, S.K., & DeVore, C.R., 2005, ApJ, in press

Kjeldseth-Moe, O. & Brekke, P. 1998, Sol. Phys., 182, 73

Kucera, T. A., Tovar, M., & De Pontieu, B. 2003 Sol. Phys., 212, 81

Landi, E., Del Zanna, G., Young, P.R., Dere, K.P., Mason, H.E., & Landini, M. 2006 ApJ, in press

Landi, E. & Landini, M. 1997, A&A, 327, 1230

Lin, Y., Engvold, O., Wiik, J.E. 2003, Sol. Phys., 216, 109

Litvinenko, Y. & Martin, S.F., 1999, Sol. Phys., 190, 45

Mazzotta P., Mazzitelli G, Colafrancesco S., & Vittorio N. 1998, A&AS Suppl., 133, 403

Mendoza-Briceño, C.A., Sigalotti, L. Di G., Erdélyi, R. 2005, ApJ, 624, 1080.

Moran, T.G. 2002, Review of Scientific Instruments, 73, 3982

Müller, D.A.N., Hansteen, V.H., & Peter, H. 2003, A&A, 411, 605

Pojoga, S. & Molowny-Horas, R. 1999, Sol. Phys., 185, 113.

Schmahl, E.J. & Orrall, F.Q., *Coronal and Prominence Plasmas*, ed: Poland, A.I., NASA Conference Publication 2442, 1986, p. 127

Schmelz, J.T., Saba, J.L.R., Strong, K.T., Winter, H.D., & Brosius, J.W. 1999, ApJ, 523, 432

Schrijver, C.J. 2001 Sol. Phys., 198, 325

Spadaro, D., Lanzafame, A. C., Consoli, L., Marsch, E., Brooks, D. H., Lang, J. 2000, A&A, 359, 716

Spadaro, D., Lanza, A.F., Lanzafame, A.C., Karpen, J.T., Antiochos, S.K., Klimchuk, J.A., & MacNeice, P.J. 2003, ApJ, 582, 486

Stellmacher, G., Koutchmy, S., & Lebecq, C. 1986, A&A, 162, 307.

Wang, Y.-M. 1999, ApJ, 520, L71

Wilhelm, K., Curdt, W., Marsch, E., et al. 1995, Sol. Phys., 162, 189

Zirker, J.B., Engvold, O., & Martin, S.F. 1998, Nature, 396, 440

---